ADVANCED MATERIALS
www.advmat.de

A p-Type Liquid-Crystal Semiconductor with Synergistic Morphological and Charge-Dynamic Modulation Enables 20.3%-Efficiency Binary Organic Solar Cells

Tianqi Chen, Yanyi Zhong, Xuehang Dong, Jiaying Wang, Wanying Feng, Jiangbin Zhang, Kai Han,* Adiljan Wupu, Weifei Fu, Bin Kan,* and Yongsheng Chen*

Solid additives serve as an effective strategy for modulating the morphology of organic solar cell (OSC) active layers, which critically linked to devices performance. However, current solid additives primarily focus on morphological control, while their inherently weak electrical characteristics may limit improvements in carrier mobility and other electrical properties. This study innovatively introduces a p-type rod-like liquid crystalline (LC) organic-semiconductor, 2-decyl-7-phenylbenzo[b]benzo[4,5]thieno[2,3-d]thiophene (Ph-BTBT-10), as a multifunctional additive in D18:L8-BO-based binary OSCs. Benefiting from its strong π-π stacking and high intrinsic mobility, Ph-BTBT-10 enables precise morphological control while simultaneously improving electrical properties. This dual effect synergistically extends exciton diffusion length, enhances charge separation, suppresses recombination, and significantly boosts hole mobility in blend films. Consequently, the optimized binary devices attained a competitive power conversion efficiency (PCE) of 20.3%, alongside a short-circuit current density of 27.28 mA cm^{-2} and fill factor of 80.5%. To the best of knowledge, this performance ranks among the highest reported for binary systems exceeding the 20% PCE threshold. This work demonstrates that p-type LC semiconductors function as multifunctional additives capable of concurrently regulating morphology and boosting intrinsic electrical properties by establishing expanded charge-transport networks, presenting a promising new paradigm for advancing OSC performance.

1. Introduction

Organic solar cells (OSCs), as the promising next generation renewable energy source, have attracted broad attentions due to their merits of lightweight, solution processability, superior flexibility and unique transparency, etc.[1–6] Recent years, the power conversion efficiencies (PCEs) of single-junction solar cells have surpassed 20% due to the innovative photovoltaic materials and device engineering.[7–12] However, there still exists an efficiency gap between OSCs and inorganic/perovskite solar cells. The performance of OSCs is critically dependent on the morphology arising from donor–acceptor interactions within the active layer. High-performance OSCs necessitate a well-defined, bi-continuous network structure with appropriate phase separation formed by the donor and acceptor materials, which directly dictates carrier collection efficiency and is intricately linked to key parameters such as short-circuit density (J_{sc}) and fill factor (*FF*). However, achieving the aforementioned ideal active layer

T. Chen, X. Dong, J. Wang, B. Kan
School of Materials Science and Engineering, National Institute for Advanced Materials
Nankai University
Tianjin 300350, China
E-mail: kanbin04@nankai.edu.cn

T. Chen, W. Feng, Y. Chen
State Key Laboratory and Institute of Elemento-Organic Chemistry, Frontiers Science Center for New Organic Matter, The Centre of Nanoscale Science and Technology and Key Laboratory of Functional Polymer Materials, Renewable Energy Conversion and Storage Center (RECAST), College of Chemistry
Nankai University
Tianjin 300071, China
E-mail: 9820240058@nankai.edu.cn

The ORCID identification number(s) for the author(s) of this article can be found under https://doi.org/10.1002/adma.202512694

DOI: 10.1002/adma.202512694

Y. Zhong, J. Zhang, K. Han
College of Advanced Interdisciplinary Studies
National University of Defense Technology
Changsha 410073, China
E-mail: hankai0071@nudt.edu.cn

J. Zhang, K. Han
Nanhu Laser Laboratory
National University of Defense Technology
Changsha 410073, China

J. Zhang
Hunan Provincial Key Laboratory of High Energy Laser Technology
National University of Defense Technology
Changsha 410073, China

A. Wupu
State Key Laboratory of Silicon and Advanced Semiconductor Materials, Department of Polymer Science and Engineering
Zhejiang University
Hangzhou 310027, China

W. Fu
Zhejiang University-Hangzhou Global Scientific and Technological Innovation Center
Hangzhou 311200, China

morphology remains fundamentally challenging, as the molecular packing behavior of donor and acceptor materials is governed by the synergistic interplay of molecular configuration and end-group interactions.[13,14]

Several effective approaches have been employed to fine-tune active layer morphology and improve photon absorption, including additive engineering, ternary strategy, and post-treatment techniques like thermal annealing.[15–17] Among these, the utilization of solid additives represents an efficient and straightforward approach to modulate the interactions of the materials within active layers.[18–20] The function of solid additives is primarily achieved via precise morphological control within the active layer. This encompasses: (i) optimization of molecular packing, guiding nanoscale phase-separation via non-covalent interactions to favor charge transport;[21–25] (ii) thermodynamic modulation, directing microphase separation during film formation to suppress excessive aggregation and minimize recombination sites.[26–28] Additionally, certain solid additives serve as morphology-stabilizing agents to inhibit phase degradation.[29,30] However, it should be noted that current solid additive strategies remain critically dependent on morphological manipulation. Given the inherently weak electrical characteristics of additives themselves, their capacity to enhance electrical properties such as carrier mobility and conductivity remains constrained, potentially limiting improvements in device J_{sc}. Consequently, the development of next-generation additives that transcend morphological control limitations while possessing enhanced intrinsic electrical properties is imperative. Such materials are anticipated to concurrently achieve precise morphological regulation and direct electrical enhancement, thereby overcoming conventional solid additive constraints and facilitating advanced OSC development.

Liquid crystal (LC) molecules exhibit long-range orientational order, and their highly ordered alignment along the long molecular axis enables directional charge transport channels that yield high charge carrier mobility.[31–36] These materials have been widely employed in electronic devices such as flat-panel displays and field-effect transistors.[37–39] In organic photovoltaic field, Schmidt-Mende et al.[40] employed the discotic LC hexaperihexabenzocoronene in combination with a perylene dye to enhance interfacial surface area and produced excellent exciton dissociation and charge transport. The electron donor materials BTR and BTR-Cl featuring a benzodithiophene core, which exhibit pronounced liquid crystalline behavior with nematic phase characteristics.[41,42] Single-junction devices based on BTR-Cl paired with Y6 achieved an impressive PCE of 13.6% in all-small-molecule OSCs.[41] In addition to spontaneously self-assemble into dynamically ordered nanostructures, a p-type LC organic semiconductor molecule also possesses exceptional hole mobility, showing promise for simultaneous morphological control and electrical performance optimization in active layers.[43]

In this study, we employed a p-type rod-like LC organic-semiconductor 2-decyl-7-phenyl-benzothienobenzothiophene (Ph-BTBT-10),[44] featuring a smectic phase,[45] into active layers as a LC additive. The benzothienobenzothiophene-fused conjugated core of Ph-BTBT-10 enables robust π-π stacking interactions. Moreover, the terminal phenyl group introduces a suitable dipole moment of 0.5 Debye, driving dipole-dipole interactions that guide the formation of highly ordered molecular packing (Figure S1, Supporting Information). This results in long-range ordered crystalline domains with low defect density, which directly enable the material's high hole mobility and potentially direct the oriented alignment of donor/acceptor molecules during film deposition.[46,47] This process establishes long-range ordered phases, thereby influencing exciton dissociation interfaces. Furthermore, the intrinsically high hole mobility of Ph-BTBT-10 could potentially establish auxiliary hole-transport pathways within the active layer.

Systematic measurements reveal that incorporating Ph-BTBT-10 concurrently modulates the molecular packing of both donor D18 and acceptor L8-BO, enhancing intermolecular interactions and guiding the active materials toward denser packing arrangements. These results lead to a bi-continuous charge-transport network with optimal phase-separated domain sizes. More importantly, Ph-BTBT-10 prolongs exciton diffusion lengths, promotes charge separation efficiency, and suppresses triplet-state formation within the active layer, collectively yielding superior charge transport dynamics. The intrinsically high charge mobility of Ph-BTBT-10 itself provides additional charge-transport pathways, significantly boosting charge carrier mobility in D18:L8-BO blend films, with particularly pronounced enhancement in hole mobility. Consequently, Ph-BTBT-10 synergistically enhances device performance through dual mechanisms of morphological control and charge-transport augmentation. Optimized D18:L8-BO binary devices processed with Ph-BTBT-10 achieve a competitive PCE of 20.3% with a J_{sc} of 27.28 mA cm^{-2} and *FF* of 80.5%. This work demonstrates that developing p-type liquid crystalline semiconductors as multifunctional additives is capable of simultaneously regulating morphology and enhancing intrinsic electrical properties through expanded charge transport networks, representing a highly promising strategy for improving the performance of OSCs.

2. Results and Discussion

The chemical structures of the polymer donor D18, non-fullerene acceptor L8-BO, and LC additive Ph-BTBT-10 are shown in **Figure 1a**. Ultraviolet-visible -near infrared (UV-Vis-NIR) absorption spectra of the pristine and blend films without and with Ph-BTBT-10 were explored to investigate the effect of Ph-BTBT-10 on their aggregation and stacking behavior. As shown in Figure 1b, the incorporation of Ph-BTBT-10 enhances the 0-0 vibronic transition intensity ($I_{0\text{-}0}$) of the D18 neat film, resulting in the $I_{0\text{-}0}/I_{0\text{-}1}$ (0 -1 vibronic transition intensity) height ratio from 1.01 for pristine D18 film to 1.10 for the modified film. This indicates enhanced pure *J* aggregation and π–π interactions within nanoscale domains, reflecting more ordered intermolecular stacking. Additionally, as seem in the absorption spectrum of L8-BO thin films (Figure 1c), the $I_{0\text{-}1}$ intensity decreased while the $I_{0\text{-}0}/I_{0\text{-}1}$ ratio increased, accompanied by a slight redshift feature. The results indicate that the LC additive Ph-BTBT-10 also promotes more ordered molecular stacking of the acceptor L8-BO. The trend in the UV-V-NIR is absorption spectra of D18:L8-BO blend films is consistent with that observed in the pure films, as depicted in Figure S2 (Supporting Information).

As revealed by fourier transform infrared spectroscopy (Figure S3, Supporting Information), the characteristic peak of Ph-BTBT-10 at 756 cm^{-1} was observed in the D18:L8-BO+Ph-BTBT-10

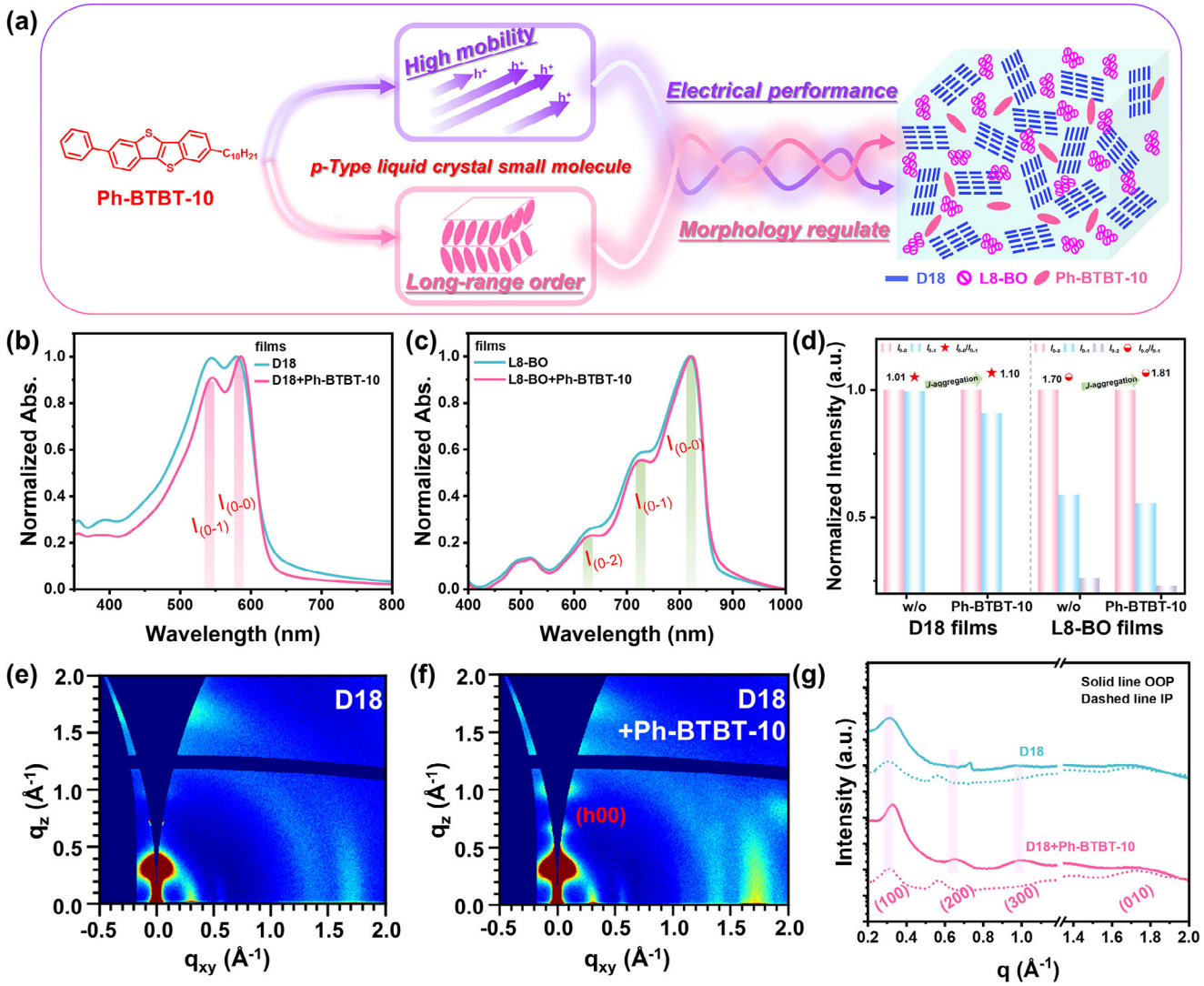

Figure 1. a) Schematic diagram of Ph-BTBT-10 dual-regulation within active layer. Normalized UV-Vis -NIR spectrum of the b) D18, and c) L8-BO films without and with additive. d) Values of $I_{0\text{-}0}/I_{0\text{-}1}$ and $I_{0\text{-}0}/I_{0\text{-}2}$ of D18 and L8-BO absorbance spectra. e,f) 2D-GIWAXS pattern of D18 films cast without and with additive. g) Out-of-plane and In-plane line cuts of D18 films.

blends and persisted after thermal annealing, indicating that Ph-BTBT-10 remains in the blend film. To further unveil its effect on the molecular packing and crystallinity behavior of donor and acceptor, the morphology of the pristine films was analyzed by grazing incidence wide-angle X-ray scattering (GIWAXS). The two-dimensional GIWAXS diffraction patterns of the neat films processed with and without LC additive Ph-BTBT-10 are depicted in Figure 1e,f and Figure S4 (Supporting Information), and the related line-cut curves are shown in Figure 1g. The (010) diffraction peaks along the out-of-plane (OOP) and in-plane (IP) directions of D18 and D18+Ph-BTBT-10 films exhibited a face-on and edge-on molecular orientation distribution with respect to the substrate. Upon the incorporation of LC additive Ph-BTBT-10, the coherence length (CL) of the D18 film was increased from 25.70 to 26.93 Å, while also exhibiting a tighter π-π stacking distance of 3.59 Å than that of control film (3.67 Å) along the OOP direction (Table S1, Supporting Information). Additionally, the Ph-BTBT-10 treated D18 film displayed high-order diffraction peaks of (200) and (300), indicating a long-range ordered crystalline structure. In addition, the L8-BO film treated with Ph-BTBT-10 additive exhibits a slight reduction in π-π stacking distance from 3.57 to 3.51 Å, indicating enhanced molecular stacking induced by the Ph-BTBT-10. Noticeably, the enhancements of CLs in both π-π stacking and lamellar stacking of D18 are more obvious than those of L8-BO, implying that Ph-BTBT-10 displays a more pronounced effect in regulating the molecular packing of D18. Generally, the optimized molecular packing of D18 and L8-BO induced by Ph-BTBT-10 is advantageous for efficient intermolecular charge transportation and desirable *FF* in the corresponding OSCs.

To gain deeper insight into the Ph-BTBT-10-assisted film formation mechanism, we performed in situ UV-vis absorption measurements on the blend films during spin-coating. The time-dependent spectral evolution is presented in **Figure** 2a,b.

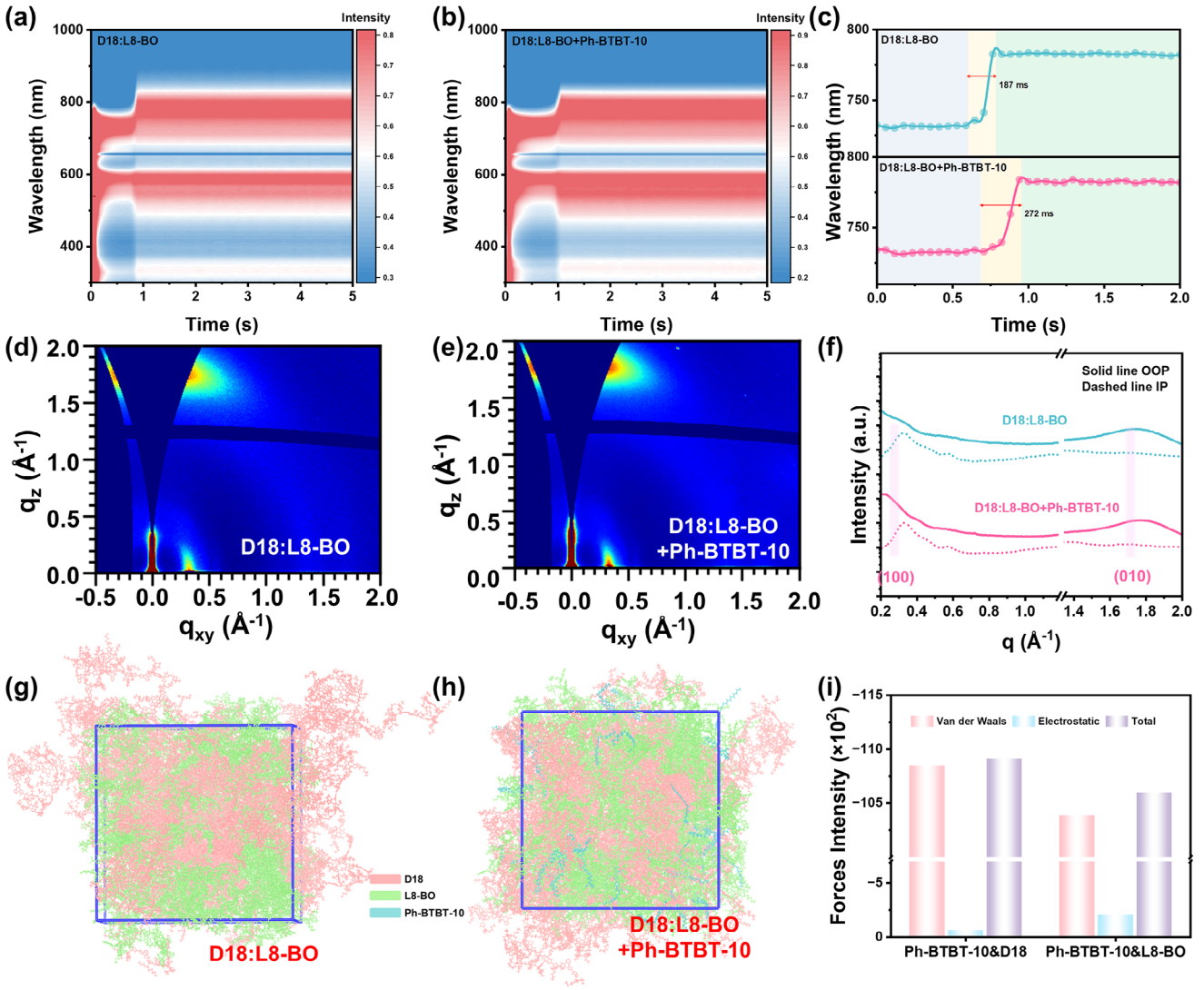

Figure 2. a,b) In situ UV-V-NIR is absorption spectra during spin-coating of the D18:L8-BO films without and with Ph-BTBT-10. c) Time evolution of acceptor peak positions. d,e) 2D-GIWAXS pattern of D18:L8-BO blend films cast without and with additive. f) Out-of-plane and In-plane line cuts of D18:L8-BO blend films. g,h) MD simulation of the blend film evolution process treated without and with Ph-BTBT-10. i) Statistical diagram of interaction analysis.

Analysis of the in situ UV-vis absorption changes revealed that the film formation process occurred in three distinct stages. Initially, the absorption peaks of all films decreased sharply and separate into donor and acceptor parts along the solvent evaporation. In the second stage, as solvent evaporation reaches critical point, donor-acceptor molecular interactions induced rapid film crystallization. Concurrently, absorption peaks progressively red-shift, with the corresponding transition time extracted from Figure 2c. Ph-BTBT-10 treated blend film exhibited extended crystallization times (from 187 to 272 ms), indicating that the incorporation of Ph-BTBT-10 could prolong the crystallization times of blends to facilitate the formation of a favorable phase separation morphology. In the third stage, the solvent has fully evaporated to form the films, resulting in constant peak positions and intensity. To further explore the effects of Ph-BTBT-10 on morphology control, in situ UV-Vis-NIR absorption under thermal annealing were employed (Figure S5, Supporting Information). The incorporation of Ph-BTBT-10 into blended films results in a time-dependent attenuation of L8-BO absorption intensity during thermal annealing, contrasting with additive-free counterparts. Mechanistic analysis reveals this behavior originates from LC-mediated restructuring of D18 molecular packing, which promotes crystalline ordering.[48] Notably, such crystallization enhancement exhibits strong consistency with the established Ph-BTBT-10 induced morphological control in D18 films, as demonstrated in prior investigations. Figure 2d–f shows the GIWAXS results and the relevant fitting data are summarized in Table S1 (Supporting Information). Both two blend films exhibit a favorable face-on dominated orientation, as confirmed by the intense (010) diffraction peaks in the OOP direction.

To further explore the interaction between LC additive Ph-BTBT-10 and active components and understand their working

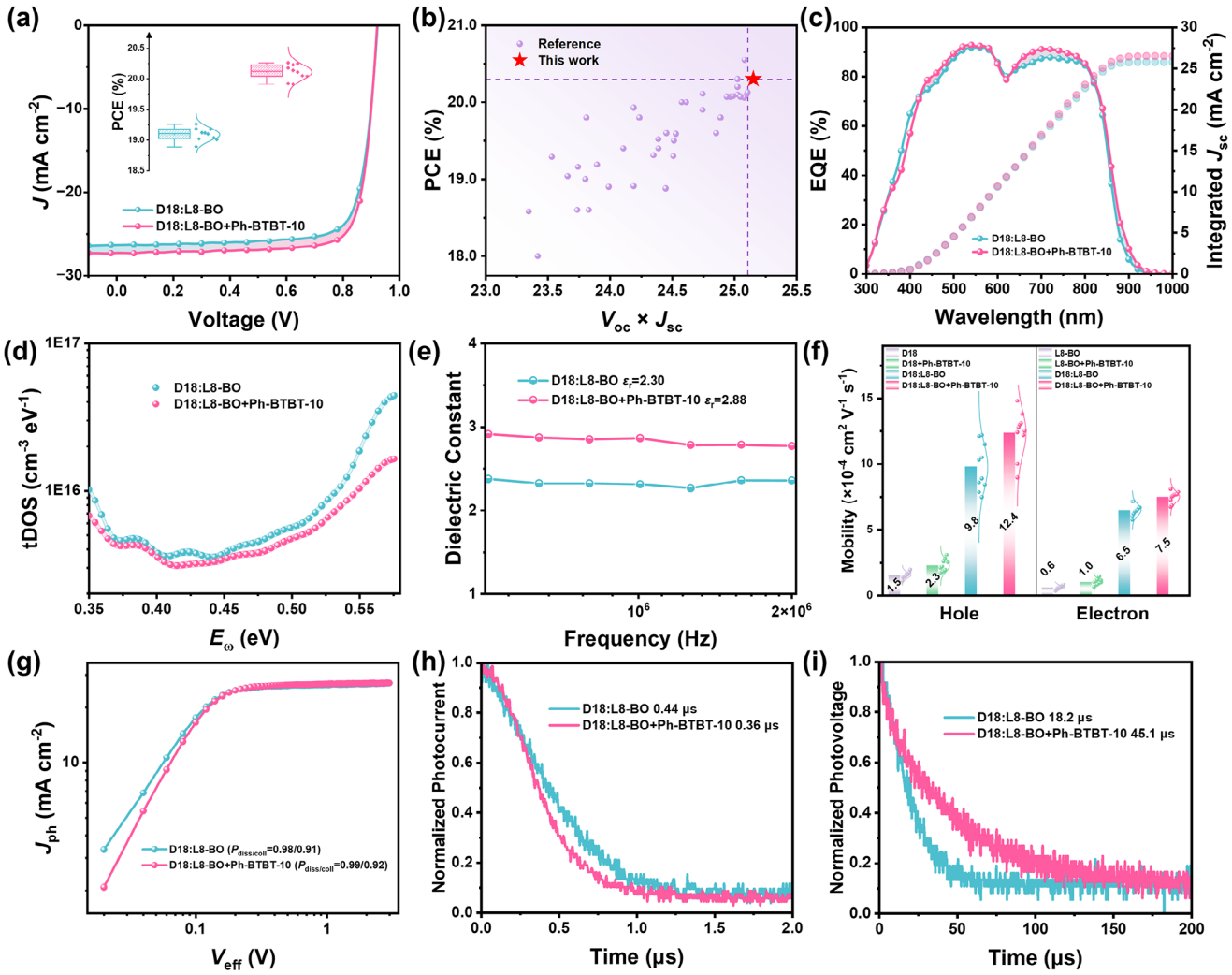

Figure 3. a) *J–V* curves of D18:L8-BO binary devices without and with Ph-BTBT-10. b) A summary of the PCE of efficient binary devices based D18:L8-BO. c) EQE curves of D18:L8-BO binary devices without and with Ph-BTBT-10. d) tDOS curves and e) dielectric properties of D18:L8-BO binary devices without and with Ph-BTBT-10. f) Charge carrier mobilities histogram. Plots of g) J_{ph} versus V_{eff}, h) TPC, and i) TPV of the devices based on D18:L8-BO without and with Ph-BTBT-10.

mechanism, a molecular dynamics approach was utilized to investigate the effect of Ph-BTBT-10 on the D18:L8-BO blends, as depicted in Figure 2g,h. Further energy analysis was performed to explore the effects of Ph-BTBT-10 on the donor and acceptor, and detailed data are summarized in Figure 2i and Tables S2,S3 (Supporting Information). Systemic analysis confirmed that incorporating Ph-BTBT-10 enhances intermolecular interactions including van der Waals forces and electrostatic interactions within the blend system, which correlates with the improved molecular stacking of D18 and L8-BO observed in prior morphological analyses, collectively demonstrating the modulatory effects of Ph-BTBT-10 on the active layer material system. Notably, intermolecular interactions between Ph-BTBT-10 and donor D18 (−10910.9 kJ mol^{-1}) are slightly stronger than those with acceptor L8-BO (−10596.1 kJ mol^{-1}). This preferential interaction likely stems from complementary electronic structures of Ph-BTBT-10's electron-rich benzothienobenzothiophene core and electron-deficient units in D18, which demonstrates consistency with the previously established UV-Vis -NIR spectroscopy and GIWAXS characterization results.

Building on the effective morphology regulation by Ph-BTBT-10, we investigated its impact on organic photovoltaic performance using devices with a conventional structure of ITO/3-BPIC-F/D18:L8-BO/PNDIT-F3N/Ag, the detailed fabrication process is provided in Table S4 (Supporting Information). The current density–voltage (*J–V*) characteristics and comprehensive photovoltaic parameters of the optimal devices are presented in **Figure 3a** and **Table 1**, respectively. The control D18:L8-BO device achieved a PCE of 19.3%, with a J_{sc} of 26.36 mA cm^{-2} and an *FF* of 79.1%. In contrast, the optimized D18:L8-BO binary device processed using Ph-BTBT-10 reached a higher PCE of 20.3%, featuring an enhanced J_{sc} of 27.28 mA cm^{-2} and an *FF* of 80.5%, among the forefront of high-efficiency OSCs (as illustrated in Figure 3b and Table S5, Supporting Information). The introduction of Ph-BTBT-10 barely reduced the V_{oc} of the device, due to its comparable energy loss (0.527 eV) to that of the

Table 1. Photovoltaic parameters of OSCs based on D18:L8-BO/PM6:L8-BO/ PM6:BTP-eC9 processed with different conditions. The average values provided in the parentheses were calculated from ten devices.

Active layer	V_{oc} [V]	J_{sc} [mA cm^{-2}]	J_{sc}^{cal} [mA cm^{-2}]	*FF* [%]	PCE [%]
D18:L8-BO	0.923	26.36	25.80	79.1	19.3
	(0.918 ± 0.003)	(26.31 ± 0.40)		(79.3 ± 1.4)	(19.1 ± 0.1)
D18:L8-BO	0.922	27.28	26.50	80.5	20.3
(Ph-BTBT-10)	(0.918 ± 0.003)	(27.19 ± 0.23)		(80.3 ± 0.5)	(20.1 ± 0.1)
PM6:L8-BO	0.900	27.42	26.40	79.4	19.6
(Ph-BTBT-10)	(0.897 ± 0.005)	(27.27 ± 0.17)		(79.0 ± 0.6)	(19.3 ± 0.2)
PM6:BTP-eC9	0.851	29.09	27.95	77.5	19.2
(Ph-BTBT-10)	(0.844 ± 0.005)	(28.90 ± 0.31)		(76.9 ± 0.6)	(18.8 ± 0.2)

reference device (0.529 eV) (Figures S6,S7 and Table S6, Supporting Information). The well-maintained high V_{oc}, combined with the simultaneously increased J_{sc} and *FF*, promoted the device's PCE from 19.3% to 20.3%. As shown in Figure 3c, the Ph-BTBT-10 treated device demonstrates enhanced external quantum efficiency (EQE) responses within 420–580 and 630–800 nm regions, indicating rather effective photo-electric conversion process in the optimized devices. This enhancement clarified different J_{sc} values derived from the *J–V* curves. The resultant integrated values of the as-cast and Ph-BTBT-10 processed devices are 25.80 and 26.50 mA cm^{-2}, respectively, which well match with the J_{sc} obtained from the *J–V* measurement with an error of less than 3%. Meanwhile, the optimized binary devices with Ph-BTBT-10 retained 84% of initial PCEs after 900 hours at 60 °C, matching the control devices (83%) (Figure S8, Supporting Information). This indicated that the introduction of small-molecule additive Ph-BTBT-10 had no adverse effect on the thermal stability of devices. Subsequently, we fabricated a 300-nm-thick device achieving a PCE of 17.0% (Figures S9,S10 and Table S7, Supporting Information). Furthermore, the Ph-BTBT-10 treated binary devices based on PM6:L8-BO and PM6:BTP-eC9 achieved PCEs of 19.6% and 19.2% (Table S8 and Figure S11, Supporting Information), respectively, demonstrating its versatility for high-performance OSCs.

To elucidate the enhanced *FF* in Ph-BTBT-10 processed devices, we initially focused on defect characterization given the detrimental role of charge trap states as the nonradiative recombination centers. Specifically, thermal admittance spectroscopy measurement was employed to study Ph-BTBT-10 mediated modulation of defect density at 298 K. As shown in Figure 3d, the results illustrated that the defect density of the device treated with Ph-BTBT-10 decreased across the entire energy range, suggesting that the Ph-BTBT-10 can restrict the defect density, which likely arises from Ph-BTBT-10 driving directional molecular stacking with active layer, thereby enhancing crystallinity.[49,50] Subsequently, we studied the effect of incorporating Ph-BTBT-10 on the dielectric constant (ϵ_r) of the D18:L8-BO blend by impedance spectroscopy. The introduction of Ph-BTBT-10 led to a larger ϵ_r value of 2.88 than that of control device (ϵ_r = 2.30), as shown in Figure 3e, which can mitigate the *FF* penalties related to the carrier loss to recombination in bulk heterojunction.[51]

The role of Ph-BTBT-10 on the charge transport properties was studied by the space-charge limited current (SCLC) method. Observation reveals that incorporation of Ph-BTBT-10 as an additive significantly enhances charge carrier transport properties within the active layer. In D18 films, Ph-BTBT-10 addition increased hole mobility (μ_h) from 1.5 to 2.3 × 10^{-4} cm^2 V^{-1} s^{-1}. Correspondingly, electron mobility (μ_e) in L8-BO films exhibited substantial improvement. The concurrent enhancement of charge transport in both donor and acceptor demonstrates Ph-BTBT-10's efficacy in optimizing intrinsic charge transport pathways. Furthermore, Ph-BTBT-10 boosts charge carrier mobilities in the D18:L8-BO blend film, elevating μ_e from 6.5 to 7.5 × 10^{-4} cm^2 V^{-1} s^{-1} while delivering a more pronounced μ_h enhancement from 9.8 to 12.4 × 10^{-4} cm^2 V^{-1} s^{-1} (Figure 3f). This enhancement is primarily attributed to the modulation of Ph-BTBT-10 in phase-separated morphology, which facilitates the formation of an optimized bicontinuous interpenetrating network. The resultant microstructure thereby establishes efficient percolation pathways for charge transport throughout the active layer. Apart from these, the influence of Ph-BTBT-10 on the exciton dissociation and charge collection process of devices was evaluated through photocurrent density (J_{ph}) versus effective voltage (V_{eff}) measurements, elevating exciton dissociation efficiency (P_{diss}) and collection efficiency (P_{coll}) from 0.98/0.91 to 0.99/0.92, as depicted in Figure 3g. These results correlate with the observed increase in ϵ_r for the modified blend films. Additionally, transient photocurrent (TPC) and transient photovoltaic (TPV) measurements were carried out to examine the trap states. As shown in Figure 3h,i, shorter charge extraction time (0.44 and 0.36 µs) and longer carrier lifetime of 18.2 and 45.1 µs are identified for the control and Ph-BTBT-10 processed devices, indicating reduced charge recombination kinetics in Ph-BTBT-10 treated devices, potentially due to slower triplet formation (see discussion below). In general, the optimized charge-transport dynamics and reduced trap-state density in the Ph-BTBT-10-modified D18:L8-BO device explain its enhanced J_{sc} and *FF*.

The atomic force electron microscope (AFM) measurements were performed to investigate the nanomorphology in the blend films. The AFM height and phase images are displayed in Figure S12 (Supporting Information) and **Figure** 4a,b, the root-mean-square surface roughness (R_q) is 1.18 nm for D18:L8-BO and 1.02 nm for the blend film with Ph-BTBT-10. The more uniform film surface attributed by Ph-BTBT-10 is beneficial for the better ohm contact, contributing to minishing the interface recombination. Besides, by fine statistical analysis along the directions of the arrow in Figure S13 (Supporting Information), a reduced fiber size was observed in D18:L8-BO treated with Ph-BTBT-10, which is 14.7 ± 4.5 nm compared 16.6 ± 3.9 nm (Figure 4c,d). The favorable morphology with appropriate

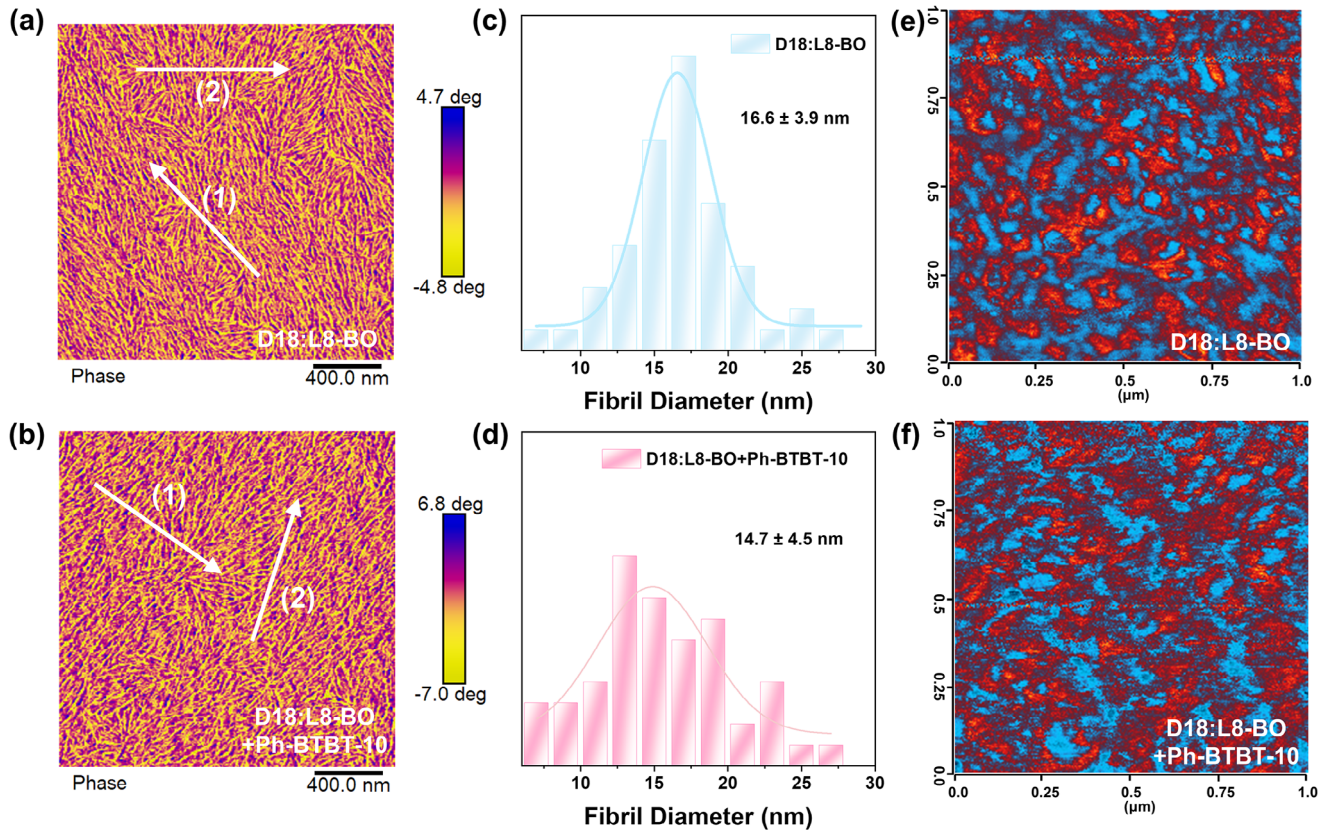

Figure 4. a,b) AFM phase images and c,d) the corresponding statistical particle size distribution diagrams. e,f) AFM-IR images of the two blend films.

domain size for D18:L8-BO with Ph-BTBT-10 is beneficial for efficient exciton dissociation with less charge recombination loss and superior charge transport. To further investigate the influence of LC additive Ph-BTBT-10 on the phase construction of active layers, the surface characteristics of blend films were analyzed carrying out microscopy-infrared spectroscopy (AFM-IR) measurement according to the absorption wavenumbers of 2216 cm^{-1} for L8-BO (red, C≡N stretching vibration). As revealed in the AFM-IR images (Figure 4e,f), the spatial distribution of donor D18 and acceptor L8-BO in the blend film demonstrates that the aggregation of L8-BO is substantially enhanced upon incorporating Ph-BTBT-10. This observation indicates that Ph-BTBT-10 effectively modulates molecular organization and promotes the formation of a bi-continuous fibrous network. Such morphology provides increased donor/acceptor interfacial areas, thereby facilitating efficient exciton dissociation and charge transport. Additionally, we conducted the contact angle tests and calculated the surface energy and the Flory-Huggins interaction parameter (χ), which shows the binary miscibility. The introduction of Ph-BTBT-10 slightly increased the χ of the system, indicating a marginal reduction in miscibility and contributing to different nanofibril diameters. This may potentially suppress excessive aggregation of pure donor/acceptor, which corroborates the AFM-IR findings showing inhibited D18 aggregation (Figures S14,S15 and Table S9, Supporting Information)

We investigate the photophysics of the neat D18 and L8-BO films using transient absorption spectroscopy (TAS) to elucidate how aggregation modulates excited-state dynamics. Upon 580 nm laser excitation, a bleach at 590 nm and photoinduced absorption (PIA) at 1180 nm were observed, assigned to the ground-state bleach (GSB) and local excitons, respectively. Notably, the D18 film treated with Ph-BTBT-10 displayed a markedly enhanced electro-absorption (EA) signal at 620 nm (**Figure** 5b), assigned to a delocalized singlet exciton. The EA enhancement correlates strongly with molecular packing, indicating reinforced π-π stacking due to Ph-BTBT-10 incorporation, which is consistent with morphological analysis previously. Further, the attenuated EA decay kinetics at 620 nm in the Ph-BTBT-10 modified D18 films favored charge transport probably (Figure S16, Supporting Information). Furthermore, we investigated the exciton diffusion length (L_D) in L8-BO via pump-fluence-dependent TAS based on exciton-exciton annihilation (EEA) kinetics (Figure S17, Supporting Information). As shown in Figures 5c and S18 (Supporting Information), Ph-BTBT-10 treatment increased L_D from 28.80 to 36.65 nm, suggesting enhanced exciton diffusion in the acceptor films, which may be attributed to suppressed exciton recombination likely from optimizing molecular ordering (Table S10, Supporting Information).

As shown in Figures 5d,e and S19 (Supporting Information), the GSB signal of the donor at 520–600 nm gradually increases along with the decay of the GSB of acceptor upon photoexcitation in both blend films, suggesting the hole-transfer behavior from the acceptor to the donor happens. The corresponding PIA signals at 620 and 1000 nm are assigned to the charge-

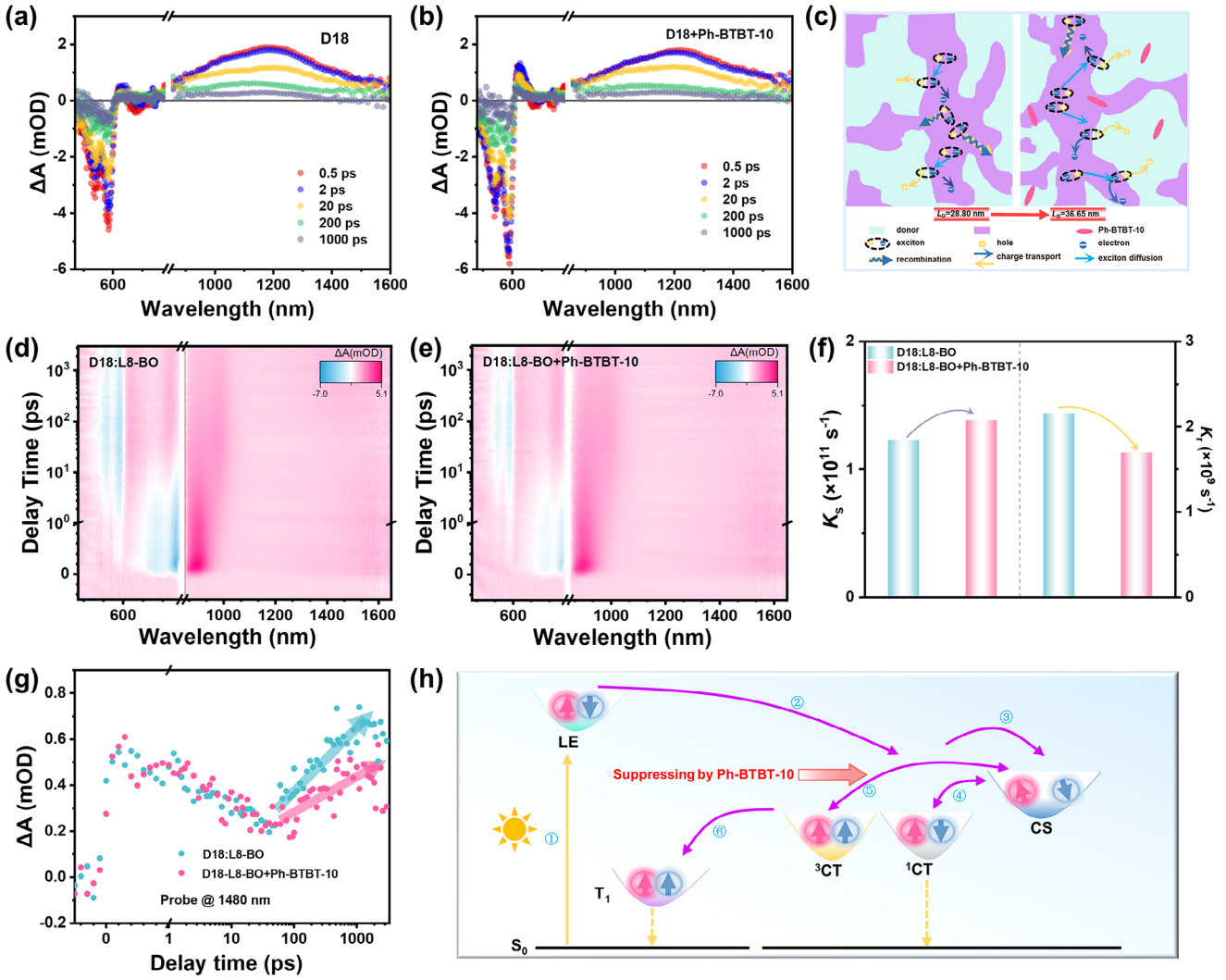

Figure 5. a,b) Transient absorption spectra (TAS) at different probe delay times of D18 films pumped at 580 nm. c) Schematic of the exciton and charge carrier behaviors for D18:L8-BO blends without and with Ph-BTBT-10. d,e) 2D TAS images of D18:L8-BO films without and with Ph-BTBT-10. f) The calculated results of K_s and K_r for D18:L8-BO films without and with Ph-BTBT-10. g) Dynamic curves probed at 1480 nm. h) Illustration of excited state dynamic in OSCs: (1) The active layer absorbs photons and is excited from the ground state (S_0) to generate local excitons (LE): (S_0-LE); (2) the formation of singlet charge-transfer (^{1}CT); (3) dissociation excitons into free charges; (4, 5) CT states formation through non-geminate recombination, possibly featuring repopulation of charge-separated (CS) state from ^{1}CT/^{3}CT (triplet charge-transfer) states concurrent with spin-allowed ^{1}CT-S_0 relaxation; (6) ^{3}CT-T_1 (triplet exciton) relaxation followed by T_1-S_0 decay via triplet-charge annihilation, resulting in irreversible depletion of photocarriers.

separated (CS) state. As shown in Figure S20 (Supporting Information), exponential fitting of the kinetic curves at 1000 nm yielded lifetimes τ_{avg} and τ for charge separation and recombination, respectively (Detailed data was summarized in Tables S11,S12, Supporting Information). And we derived the separation and recombination rates ($K_s = 1/\tau_{avg}$, $K_r = 1/\tau$) as shown in Figure 5f. We found the blend film treated with Ph-BTBT-10 exhibited an enhanced K_s and decreased K_r, indicating the Ph-BTBT-10 could promote the exciton separation and suppress the recombination in the active layers. The CS state undergoes partial recombination at the interface via back charge transfer through triplet charge-transfer (^{3}CT) states, as shown in Figure 5h, forming spin-triplet excitons (^{1}T) on the acceptor characteristic by ≈1480 nm PIA.[52] Correspondingly, TA dynamics probed at 1480 nm demonstrate suppressed ^{1}T generation kinetics and yield within 30–300 ps in Ph-BTBT-10 treated blends versus controls (Figure 5g).[53] This attenuation may be a reason for the enhanced photocurrent in D18:L8-BO device processed by Ph-BTBT-10. Mechanistically, optimized charge transport networks induced by Ph-BTBT-10 modification simultaneously mitigate recombination losses and impedes triplet-generation pathways.

3. Conclusion

This work demonstrates that incorporating the liquid crystalline molecule Ph-BTBT-10 as an additive in photoactive layers enables precise nanomorphology control and enhanced photovoltaic

performance. Systematic investigations reveal strong interactions exist between Ph-BTBT-10 and donor as well acceptor, which provides intrinsic driving forces for optimized donor and acceptor alignment, yielding compact and ordered molecular stacking. The resulting bi-continuous interpenetrating fibrillar network with optimal phase separation promotes exciton dissociation while suppressing recombination losses and triplet exciton formation kinetics. Furthermore, Ph-BTBT-10 mediated molecular ordering synergized with its inherent high charge mobility significantly enhances carrier transport in both neat and blend films. Consequently, Ph-BTBT-10 processed D18:L8-BO binary devices achieve a competitive PCE of 20.3% with J_{sc} of 27.28 mA cm^{-2} and *FF* of 80.5%. Following 900 h thermal aging at 60 °C, the Ph-BTBT-10 treated devices retained over 80% initial PCEs, which is comparable to the control devices, indicating that incorporating the small-molecule LC additive imposed no deleterious effects on thermal stability. The universality of Ph-BTBT-10 is validated in PM6:L8-BO (PCE = 19.6%) and PM6:BTP-eC9 (PCE = 19.2%) systems, establishing its broad applicability. Our study highlights the dual functionality of LC additive (for example, Ph-BTBTB-10) in concurrently regulating nanomorphology and electronic properties, mechanistically underpinned by its role in facilitating exciton dissociation, suppressing recombination pathways, and attenuating triplet-mediated energy loss channels.

Supporting Information

Supporting Information is available from the Wiley Online Library or from the author.

Acknowledgements

The authors gratefully acknowledge the financial support from the Ministry of Science and Technology of the People's Republic of China (2023YFE0210400), National Natural Science Foundation of China (22361132530, and 52303237), Natural Science Foundation of Tianjin (24JCYBJC01540), and the Fundamental Research Funds for the Central Universities of Nankai University (023-63253172).

Conflict of Interest

The authors declare no conflict of interest.

Data Availability Statement

The data that support the findings of this study are available in the supplementary material of this article.

Keywords

charge dynamics, liquid-crystal semiconductor, morphology regulation, organic solar cells, power conversion efficiency

Received: July 3, 2025
Revised: August 3, 2025
Published online:

[1] J. Yi, G. Zhang, H. Yu, H. Yan, *Nat. Rev. Mater.* **2024**, *9*, 46.
[2] H. Jinno, K. Fukuda, X. Xu, S. Park, Y. Suzuki, M. Koizumi, T. Yokota, I. Osaka, K. Takimiya, T. Someya, *Nat. Energy* **2017**, *2*, 780.
[3] S. Li, Z. Li, X. Wan, Y. Chen, *eScience* **2023**, *3*, 100085.
[4] P. Cheng, G. Li, X. Zhan, Y. Yang, *Nat. Photonics* **2018**, *12*, 131.
[5] M. Kaltenbrunner, M. S. White, E. D. Głowacki, T. Sekitani, T. Someya, N. S. Sariciftci, S. Bauer, *Nat. Commun.* **2012**, *3*, 770.
[6] H. Tang, Y. Liang, C. Liu, Z. Hu, Y. Deng, H. Guo, Z. Yu, A. Song, H. Zhao, D. Zhao, Y. Zhang, X. Guo, J. Pei, Y. Ma, Y. Cao, F. Huang, *Nature* **2022**, *611*, 271.
[7] X. Dai, B. Fan, X. Xu, Q. Peng, *Adv. Mater.* **2025**, *37*, 2503072.
[8] S. Gao, S. Xu, C. Sun, L. Yu, J. Li, R. Li, X. Liu, X. Zhou, H. Chen, Y. Lin, X. Bao, W. Zhu, X. Song, *Adv. Mater.* **2025**, *37*, 2420631.
[9] C. Xu, J. Yang, S. Gámez-Valenzuela, J.-W. Lee, J. Che, P. Chen, G. Zhang, D. Hu, Y. Wang, J. Lv, Z. Zhong, X. Chen, G. Zhang, F. Zhao, B. J. Kim, X. Guo, B. Liu, *Energy Environ. Sci.* **2025**, *18*, 5913.
[10] L. Wang, C. Chen, Y. Fu, C. Guo, D. Li, J. Cheng, W. Sun, Z. Gan, Y. Sun, B. Zhou, C. Liu, D. Liu, W. Li, T. Wang, *Nat. Energy* **2024**, *9*, 208.
[11] J. Wang, P. Wang, T. Chen, W. Zhao, J. Wang, B. Lan, W. Feng, H. Liu, Y. Liu, X. Wan, G. Long, B. Kan, Y. Chen, *Angew. Chem., Int. Ed.* **2025**, *64*, 202423562.
[12] R. Ma, Z. Luo, Y. Zhang, L. Zhan, T. Jia, P. Cheng, C. Yan, Q. Fan, S. Liu, L. Ye, G. Zhang, X. Xu, W. Gao, Y. Wu, J. Wu, Y. Li, Y. Liu, F. Liu, J. Song, H. Chen, W. Chen, X. Zhang, Y. Liu, J. Yuan, Q. Liu, Z. Kan, H. Yin, X. Li, Y. Ma, D. Deng, et al., *Sci. China Mater.* **2025**, *68*, 1689.
[13] G. F. A. Dibb, F. C. Jamieson, A. Maurano, J. Nelson, J. R. Durrant, *J. Phys. Chem. Lett.* **2013**, *4*, 803.
[14] S. R. Cowan, A. Roy, A. J. Heeger, *Phys. Rev. B* **2010**, *82*, 245207.
[15] Y. Xu, J. Wang, T. Zhang, Z. Chen, K. Xian, Z. Li, Y.-H. Luo, L. Ye, X. Hao, H. Yao, J. Hou, *Energy Environ. Sci.* **2023**, *16*, 5863.
[16] Y. Wang, K. Sun, C. Li, C. Zhao, C. Gao, L. Zhu, Q. Bai, C. Xie, P. You, J. Lv, X. Sun, H. Hu, Z. Wang, H. Hu, Z. Tang, B. He, M. Qiu, S. Li, G. Zhang, *Adv. Mater.* **2024**, *36*, 2411957.
[17] J. Min, X. Jiao, V. Sgobba, B. Kan, T. Heumüller, S. Rechberger, E. Spiecker, D. M. Guldi, X. Wan, Y. Chen, H. Ade, C. J. Brabec, *Nano Energy* **2016**, *28*, 241.
[18] D. He, L. Xie, Y. Bai, H. Zhang, L. Liu, J. Kong, Y. Chai, X. Li, M. Wang, Y. Zhang, J. Zhang, Y. Li, F. Gao, D. M. Guldi, F. Zhao, *Angew. Chem., Int. Ed.* **2025**, *64*, 202505722.
[19] Q. Chen, Z. Bian, Y. Yang, X. Cui, C. Jeffreys, X. Xu, W. Li, Y. Liu, M. Heeney, Z. Bo, *Angew. Chem., Int. Ed.* **2024**, *63*, 202405949.
[20] T. Chen, Y. Bai, X. Ji, W. Feng, T. Duan, X. Jiang, Y. Yi, J. Yu, G. Lu, X. Wan, B. Kan, Y. Chen, *Nano Energy* **2024**, *125*, 109604.
[21] L. Liu, H. Li, J. Xie, Z. Yang, Y. Bai, M. Li, Z. Huang, K. Zhang, F. Huang, *Adv. Mater.* **2025**, *37*, 2500352.
[22] H. Li, L. Liu, J. Yu, J. Xie, Y. Bai, Z. Yang, M. Dong, K. Zhang, F. Huang, Y. Cao, *Adv. Funct. Mater.* **2025**, 2505226.
[23] C. Li, M. Deng, H. Chen, Y. Duan, C. Liao, Z. Chen, Q. Peng, *Energy Environ. Sci.* **2025**, *18*, 5564.
[24] S. Wang, S. Wang, J. Wang, N. Yu, J. Qiao, X. Xie, C. Li, M. S. Abbasi, R. Ding, X. Zhang, Y. Han, G. Lu, J. Zhang, X. Hao, Z. Tang, Y. Cai, H. Huang, *Adv. Energy Mater.* **2025**, 2405205.
[25] T. Chen, Y. Zhong, T. Duan, X. Tang, W. Zhao, J. Wang, G. Lu, G. Long, J. Zhang, K. Han, X. Wan, B. Kan, Y. Chen, *Angew. Chem., Int. Ed.* **2025**, *64*, 202412983.
[26] L. Guo, J. Song, J. Deng, J. Qiao, J. Zhang, C. Li, S. Yuan, B. Han, M. H. Jee, Z. Ge, C. Zhang, G. Lu, X. Hao, H. Y. Woo, Y. Sun, *Adv. Mater.* **2025**, *37*, 2504396.
[27] W. Xiong, Y. Cui, Z. Zhang, S. Zhu, Z. Wang, Z. Chai, H. Hu, Y. Chen, *Angew. Chem., Int. Ed.* **2025**, *64*, 202500085.

[28] N. Wei, H. Lu, Y. Wei, Y. Guo, H. Song, J. Chen, Z. Yang, Y. Cheng, Z. Bian, W. Zhang, Q. Chen, Y. Liu, W. Zhao, X. Xu, Z. Bo, *Energy Environ. Sci.* **2025**, *18*, 2298.
[29] Y.-T. Wang, W.-J. Sun, Y. Zhang, B.-Y. Zhang, Y.-T. Ding, Z.-Q. Zhang, L. Meng, K. Huang, W. Ma, H.-L. Zhang, *Angew. Chem., Int. Ed.* **2025**, *64*, 202417643.
[30] S. Luo, Y. Dou, X. Shi, Y. Liu, T. Liu, X. Hu, T. Li, X. Peng, H. Hu, H. Yan, S. Chen, *Adv. Mater.* **2024**, *36*, 2407609.
[31] Y.-C. Lin, G.-S. Li, P.-J. Yu, E. Ercan, W.-C. Chen, *J. Chin. Chem. Soc.* **2022**, *69*, 1289.
[32] T. Kato, J. Uchida, T. Ichikawa, T. Sakamoto, *Angew. Chem., Int. Ed.* **2018**, *57*, 4355.
[33] H. Iino, J.-i. Hanna, *Adv. Mater.* **2011**, *23*, 1748.
[34] K. Takimiya, S. Shinamura, I. Osaka, E. Miyazaki, *Adv. Mater.* **2011**, *23*, 4347.
[35] V. Coropceanu, J. Cornil, D. A. da Silva Filho, Y. Olivier, R. Silbey, J.-L. Brédas, *Chem. Rev.* **2007**, *107*, 926.
[36] F. Padinger, R. S. Rittberger, N. S. Sariciftci, *Adv. Funct. Mater.* **2003**, *13*, 85.
[37] H. Iino, J.-i. Hanna, *Polym. J.* **2017**, *49*, 23.
[38] R. Raveendran, M. Nagaraj, M. A. G. Namboothiry, *ACS Appl. Electron. Mater.* **2020**, *2*, 3336.
[39] M. Mitov, *Adv. Mater.* **2012**, *24*, 6260.
[40] L. Schmidt-Mende, A. Fechtenkötter, K. Müllen, E. Moons, R. H. Friend, J. D. MacKenzie, *Science* **2001**, *293*, 1119.
[41] H. Chen, D. Hu, Q. Yang, J. Gao, J. Fu, K. Yang, H. He, S. Chen, Z. Kan, T. Duan, C. Yang, J. Ouyang, Z. Xiao, K. Sun, S. Lu, *Joule* **2019**, *3*, 3034.
[42] K. Sun, Z. Xiao, S. Lu, W. Zajaczkowski, W. Pisula, E. Hanssen, J. M. White, R. M. Williamson, J. Subbiah, J. Ouyang, A. B. Holmes, W. W. H. Wong, D. J. Jones, *Nat. Commun.* **2015**, *6*, 6013.
[43] Y. He, M. Sezen, D. Zhang, A. Li, L. Yan, H. Yu, C. He, O. Goto, Y.-L. Loo, H. Meng, *Adv. Electron. Mater.* **2016**, *2*, 1600179.
[44] H. Iino, T. Usui, J.-i. Hanna, *Nat. Commun.* **2015**, *6*, 6828.
[45] I. Wurzbach, C. Rothe, K. Bruchlos, S. Ludwigs, F. Giesselmann, *J. Mater. Chem. C* **2019**, *7*, 2615.
[46] X. Liao, Q. He, G. Zhou, X. Xia, P. Zhu, Z. Xing, H. Zhu, Z. Yao, X. Lu, Y. Chen, *Chem. Mater.* **2021**, *33*, 430.
[47] Z. Jia, Y. Wei, X. Wang, S. Hu, K. Yao, F. Li, *Chem. Phys. Lett.* **2016**, *661*, 119.
[48] W. Feng, Y. Bai, J. Wang, S. Yuan, X. Wan, Y. Chen, B. Kan, Y. Chen, *Chin. J. Chem.* **2024**, *42*, 3075.
[49] H. Wang, Y. Zheng, G. Zhang, P. Wang, X. Sui, H. Yuan, Y. Shi, G. Zhang, G. Ding, Y. Li, T. Li, S. Yang, Y. Shao, *Adv. Mater.* **2024**, *36*, 2307855.
[50] S. Wang, P. Kaienburg, B. Klingebiel, D. Schillings, T. Kirchartz, *J. Phys. Chem. C* **2018**, *122*, 9795.
[51] S. Park, S. Yoon, H. Ahn, H. Yu, E.-Y. Shin, K. Cho, Y. H. Jang, Y. Jun, H. J. Son, *Joule* **2025**, *9*, 101927.
[52] K. Jiang, J. Zhang, C. Zhong, F. R. Lin, F. Qi, Q. Li, Z. Peng, W. Kaminsky, S.-H. Jang, J. Yu, X. Deng, H. Hu, D. Shen, F. Gao, H. Ade, M. Xiao, C. Zhang, A. K. Y. Jen, *Nat. Energy* **2022**, *7*, 1076.
[53] H. Gao, Q. Li, B. Fan, Z. Bi, W. Jiang, S. Zhang, Q. Fan, T. Chen, F. R. Lin, B. Kan, D. Lei, W. Ma, A. K.-Y. Jen, *Adv. Energy Mater.* **2024**, 2403121.